Journal of Materials Chemistry A

Supporting Information

for

Synthesis, characterization and DFT studies of zinc-doped copper oxide nanocrystals for gas sensing applications

V. Cretu,[a] V. Postica,[a] A. K. Mishra,[b,‡] M. Hoppe,[c] I. Tiginyanu,[a] Y. K. Mishra,[c] L. Chow,[d] Nora H. De Leeuw,[b,e,‡] R. Adelung,[c,†] and O. Lupan,[c,‖]

[a] *Department of Microelectronics and Biomedical Engineering, Technical University of Moldova, Chisinau, Republic of Moldova.*
[b] *Department of Chemistry, University College London, 20 Gordon Street, London WC1H 0AJ, U.K.*
[c] *Faculty of Engineering, Institute for Materials Science, Christian-Albrechts Universität zu Kiel, Kaiserstr. 2, D-24143, Kiel, Germany.*
[d] *Department of Physics, University of Central Florida, Orlando, FL 32816-2385, USA.*
[e] *School of Chemistry, Cardiff University, Main Building, Park Place, Cardiff CF10 3AT, U.K.*
† e-mail ra@tf.uni-kiel.de.
‡ e-mail n.h.deleeuw@ucl.ac.uk deleeuwn@cardiff.ac.uk abhishek.mishra@ucl.ac.uk
‖ Corresponding author: Professor Dr. LUPAN Oleg e-mail ollu@tf.uni-kiel.de lupanoleg@yahoo.com

Received ZZZ, revised ZZZ, accepted ZZZ
Published online ZZZ (Dates will be provided by the publisher.)

Keywords Nanocrystalline materials, cuprite, tenorite, hydrogen gas sensor.

Figure-S1

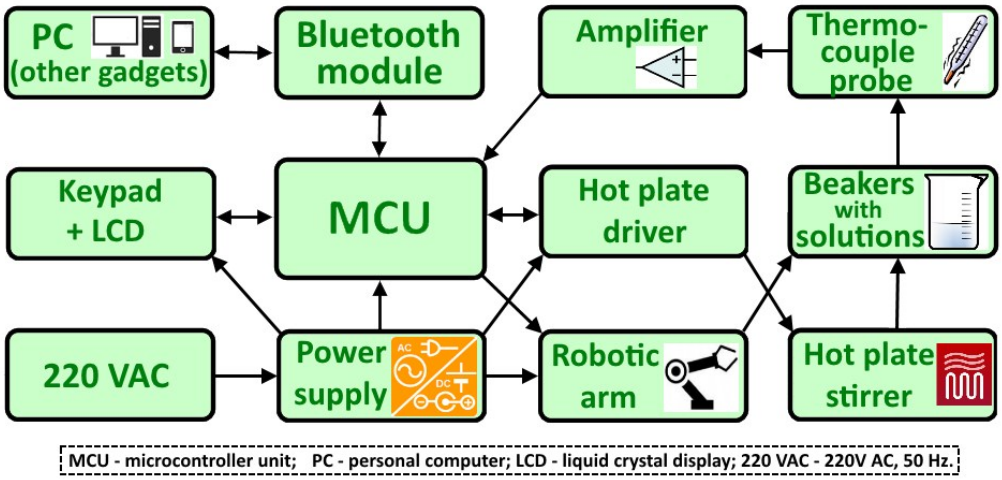

Figure S1. Block diagram of the chemical solution deposition system based on robotic arm controlled by a microcontroller.

The deposition system is composed of the following modules:

1. MCU – microcontroller unit that interface directly with the robot's servos (which are used for arm articulations control), hot plate driver for temperature control in beakers through a PID controller, input/output signals (keypad and LCD), and Bluetooth module for communication with personal computer (PC) or other gadgets (such as smartphones) through a graphic user interface (GUI).
2. Bluetooth module – is used for wireless communication between MCU and PC through a GUI.
3. PC or other gadgets – represents the PC or other gadgets which support GUI for control a robotic arm (to send commands and to monitor the systems parameters such as temperature in beakers, numbers of performed SCS cycles, time of deposition, duration of substrate immersion in beakers, etc.).
4. Keypad + LCD – represents an input/output module (a keypad + LCD display) for display of system parameters information and sending commands.
5. 220 VAC – primary power supply (220 V, AC, 50 Hz).
6. Power supply – secondary DC power supply (+5 V, - 5 V, + 12 V) for system modules.
7. Hot plate driver – triac and optocoupler based driver of hot plate stirrer for beakers temperature control through a PID controller (25 – 99 ºC).
8. Hot plate stirrer – represents a hot plate stirrer on which are placed beakers to maintain a necessary temperature of complex solutions during the deposition process.
9. Beakers with solution – represents a thermo-resistant glass beakers with complex anionic and cationic solutions which are maintained at necessary conditions.
10. Thermocouple probe – represents a thermocouple probe for liquid solutions which is used for temperature monitoring in the complex solutions.
11. Amplifier – is an operational amplifier based circuit to amplify the signal from thermocouple probe for further signal processing in PID controller.
12. Robotic arm – represents an articulated type robotic arm based on servos which perform the dipping of substrate in beakers with anionic and cationic complex solutions by a predefined algorithm with introduced parameters from input/output system or GUI.

Figure-S2

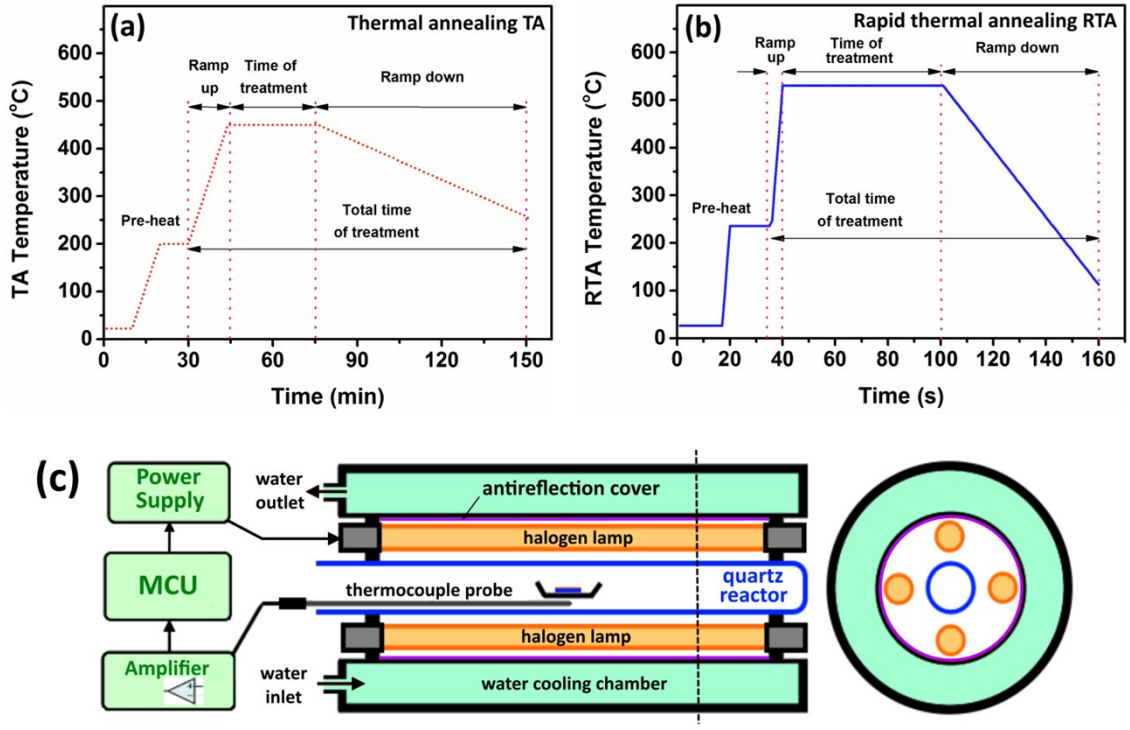

Figure S2. A typical schematic temperature profile of: (a) thermal annealing TA process at 450 °C; and (b) rapid thermal annealing RTA process at 525 °C. (c) Schematic diagram of the rapid thermal annealing (RTA) system.

In both cases the reactors are pre-heated to 200 °C and then samples are introduced for annealing process. Temperature ramp rate for electrical furnace was ~ 18 °C/min, thus ramp up time to install 450 °C in reactor was ~ 15 min. In this work, the time of treatment is not total time of annealing, but the duration of films treatment at an indicated temperature, as can be seen from **Figure S2a**. For 30 min time of treatment, the total time of annealing was 120 min, and can be calculated by time of treatment × 4. Temperature decrease rate of electrical furnace was ~ 2.6 °C/min.

For RTA treatment (**Figure S2b**), temperature rise rate was very fast (~ 65 °C/s), thus with pre-heat at 200 °C the ramp up time to reach 525 °C in reactor was ~ 5 s. Temperature drop rate of RTA system was, as well as, very fast ~ 6 °C/s, due to water cooling system. Time of annealing process was defined like in case of TA-treatment, but total rapid annealing time was time of treatment × 2. In both cases, samples are extracted at the end of total annealing time according to **Figure S2**. However in the case of RTA treatment the ramp down period have very little influences on structural, morphological and chemical properties of the nano-crystallite copper oxide films (not shown here) due to rapid decrease of temperature, thus it is not an important factor in our investigations.

In **Figure S2c** schematic diagram of the rapid thermal annealing (RTA) system is presented as cross-sectional view. Sample is placed in a quartz reactor where temperature is monitored continuously by thermocouple probe. Temperature inside quartz reactor is controlled by a microcontroller unit (MCU) using on-off controller. The four halogen lamps (5 kW) are used for rapid increase of temperature in quartz reactor. For higher thermal efficiency, the inside of the water cooling chamber is a covered with a polished metal surface antireflection layer.

Figure-S3

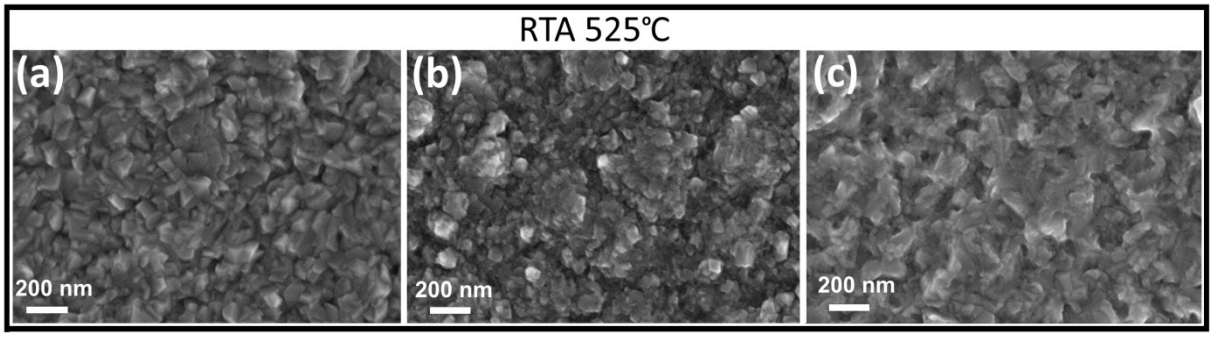

Figure S3. SEM images of the RTA treated copper oxide nano-crystallite films with zinc concentration: (a) – (#1 or c1) – 1.9 wt% Zn; (b) – (#2 or c2) – 2.7 wt% Zn; (c) – (#3 or c3) – 3.0 wt% Zn.

Figure-S4

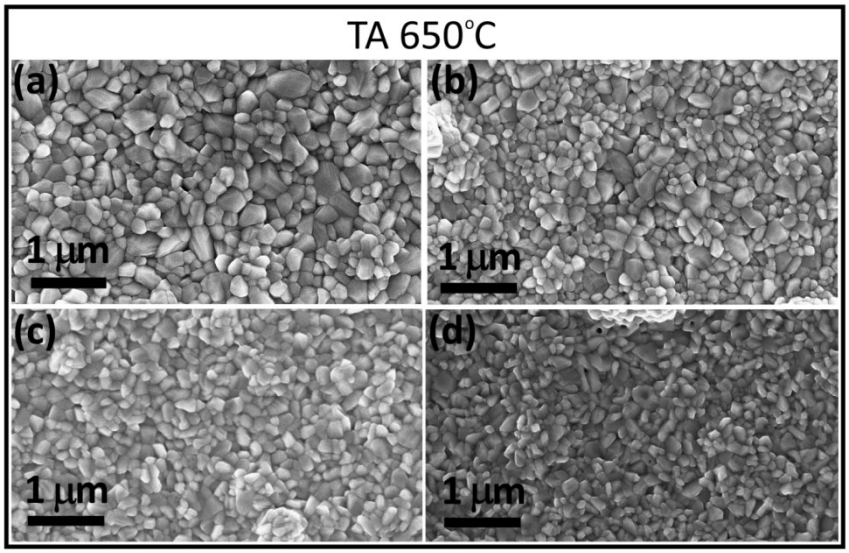

Figure S4. SEM images of the TA treated copper oxide nano-crystallite films with zinc concentration: (a) – (0); (b) – (#1 or c1) – 1.9 wt% Zn; (c) – (#2 or c2) – 2.4 wt% Zn; (d) – (#3 or c3) – 2.8 wt% Zn.

Figure-S5

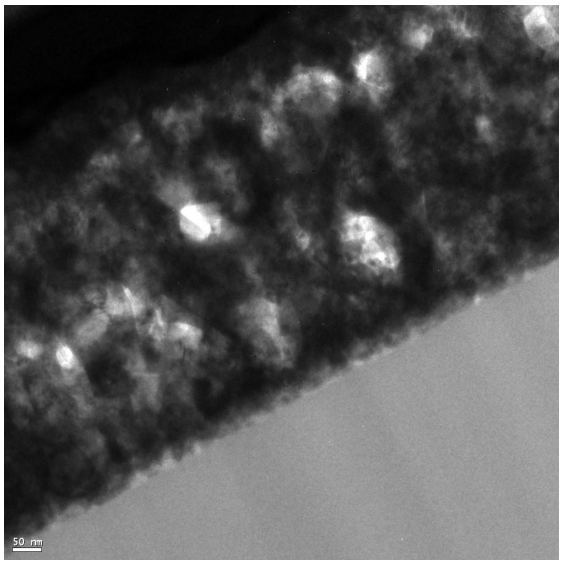

Figure S5. TEM image of the RTA treated copper oxide nano-crystallite films with zinc concentration–(3).

Figure-S6

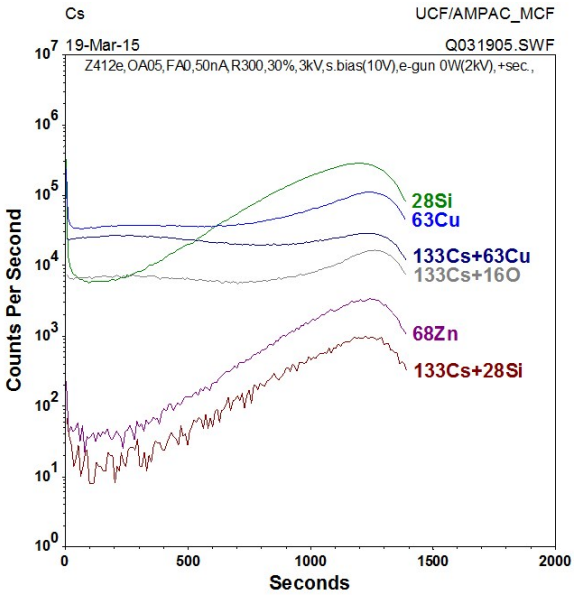

Figure S6 Shows the secondary ion mass spectrometry SIMS measurement of the Zn-doped CuO thin film. The CuO:Zn thin film on the substrate was in the form of nanocrystals. The SIMS result shows that while the concentrations of Cu or O remain constant as a function of depth, the Zn concentration varies rapidly as a function of depth and its behavior seems to track that of the Si substrate. Therefore we conclude that the SIMS signal of Zn maybe contaminated by the Si signal.

Figure-S7

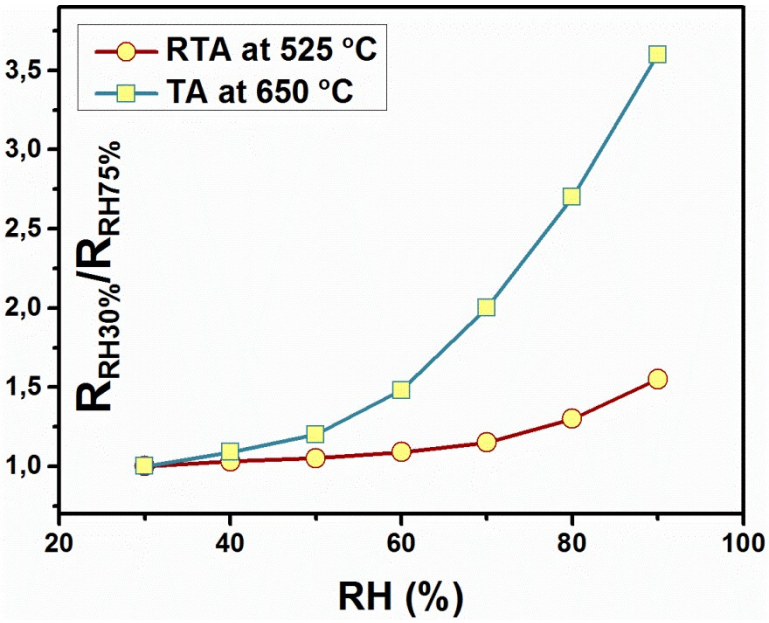

Figure S7. Response of the sensors based on samples treated RTA at 525 °C and TA at 650 °C versus RH value. Response was defined as the ratio of resistance in 30% RH ($R_{RH30\%}$) and 90% RH ($R_{RH90\%}$).

Figure-S8

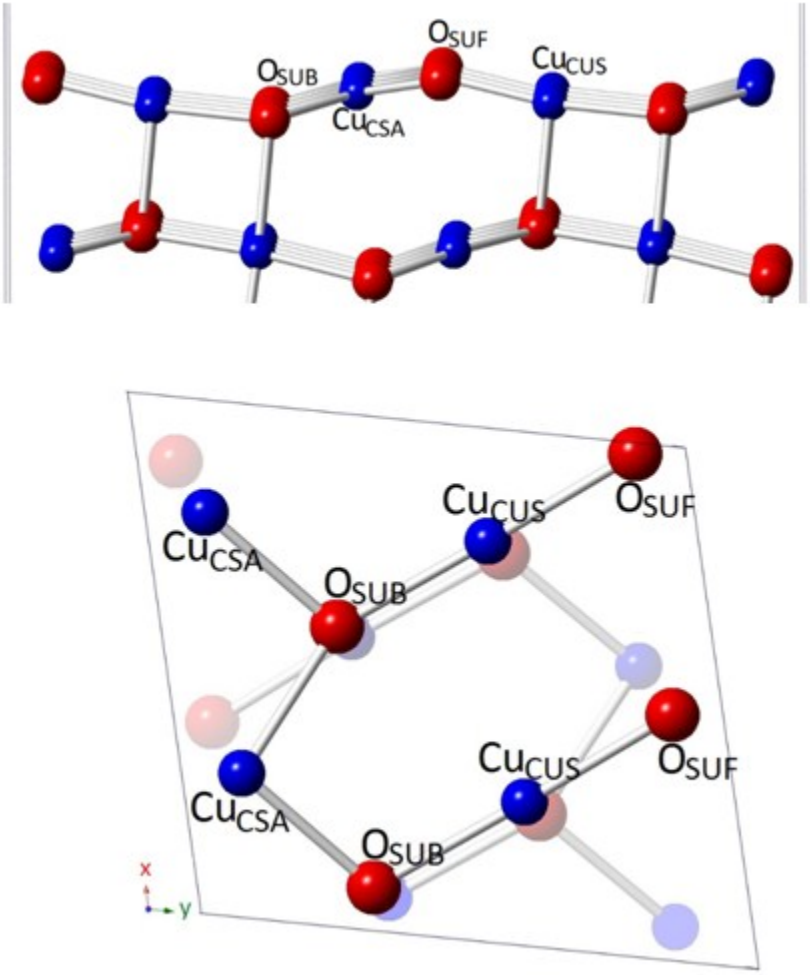

Figure S8. Side (upper panel) and top views of the CuO(111) surface.

The (111) surface is the most stable surface and found to be dominant in the CuO crystal morphology.[9] The top layer consists of 3- and 4-coordinated Cu and O atoms. 3-coordinated O atoms (O_{SUF}) are the most exposed atoms, each connected to one 3-coordinated (coordinatively unsaturated -Cu_{CUS}) and two 4-coordinated (coordinatively saturated - Cu_{CSA}) Cu atoms.

Figure-S9

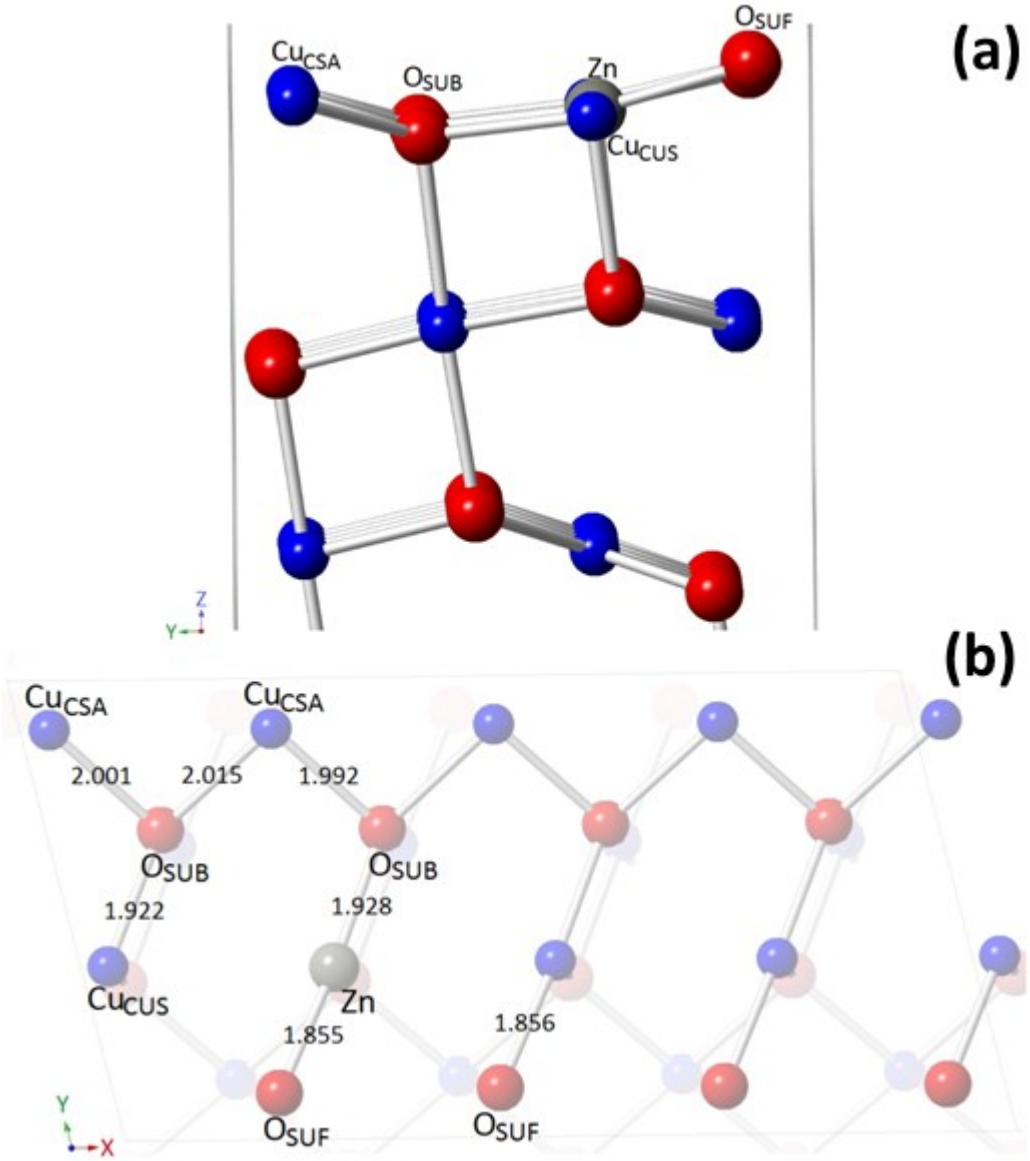

Figure S9. Side (a) and top (b) views of the Zn-doped (2×1) slab of the CuO(111) surface. Bond length values are in Å.

Figure-S10

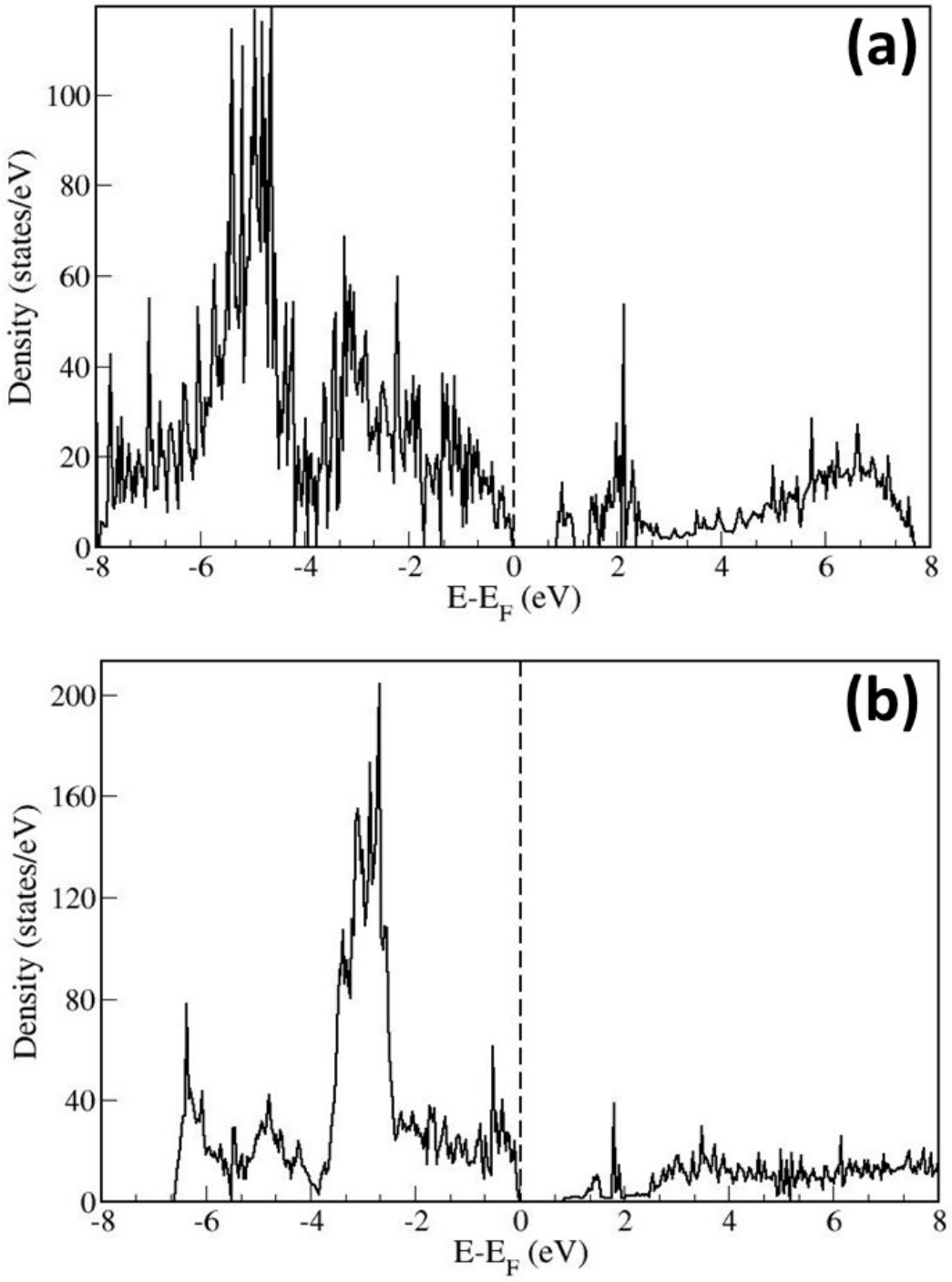

Figure S10. (a) Electronic density-of-states (DOS) of the systems of (a) the H_2 molecule adsorbed on the Zn-doped CuO(111) surface, and (b) the H_2 molecule adsorbed on the Zn-doped $Cu_2O(111)$-Cu_{vac} surface, with Fermi-level set to zero. Dashed lines show the Fermi-level.

Figure-S11

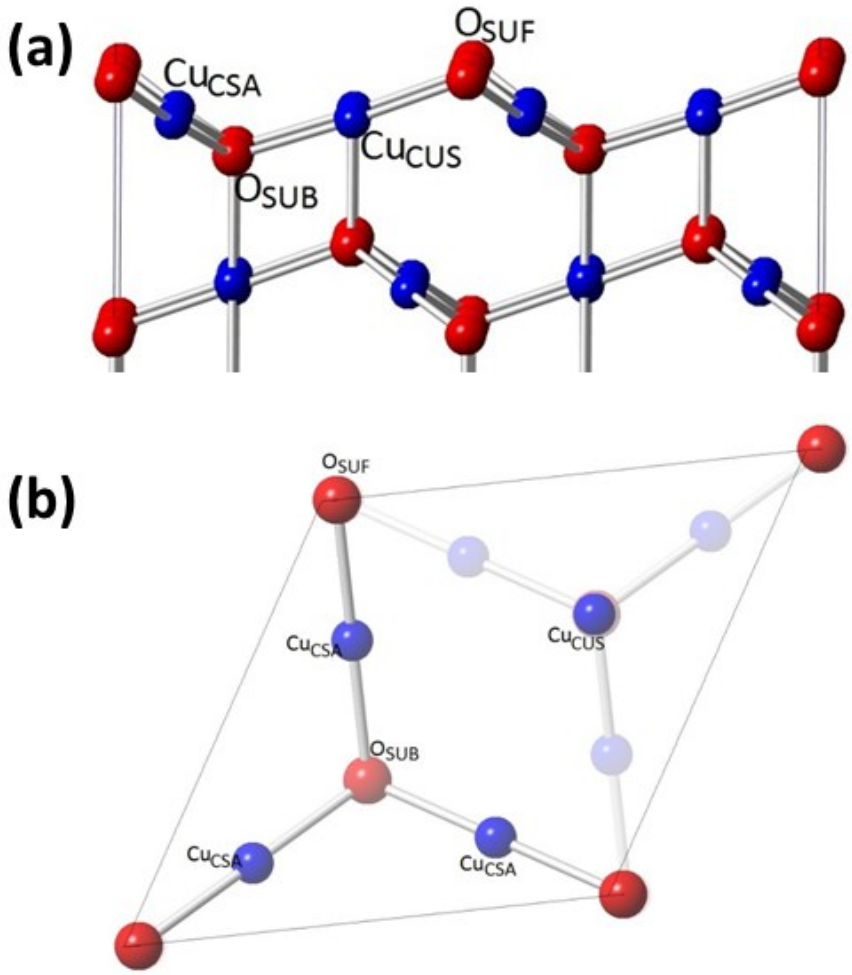

Figure S11. Side (a) and top (b) views of $Cu_2O(111)$ surface.

The oxygen-terminated $Cu_2O(111)$ surface is the most stable surface among the different low-index surfaces of Cu_2O [17], consisting of four different atomic sites in the top layer, namely a coordinatively unsaturated copper Cu_{CUS}, an outermost oxygen $O_{SUF,}$ a coordinatively saturated copper Cu_{CSA} and a sub-surface oxygen atom O_{SUB}, which is 4-fold coordinated as shown in Fig. S11.

Figure-S12

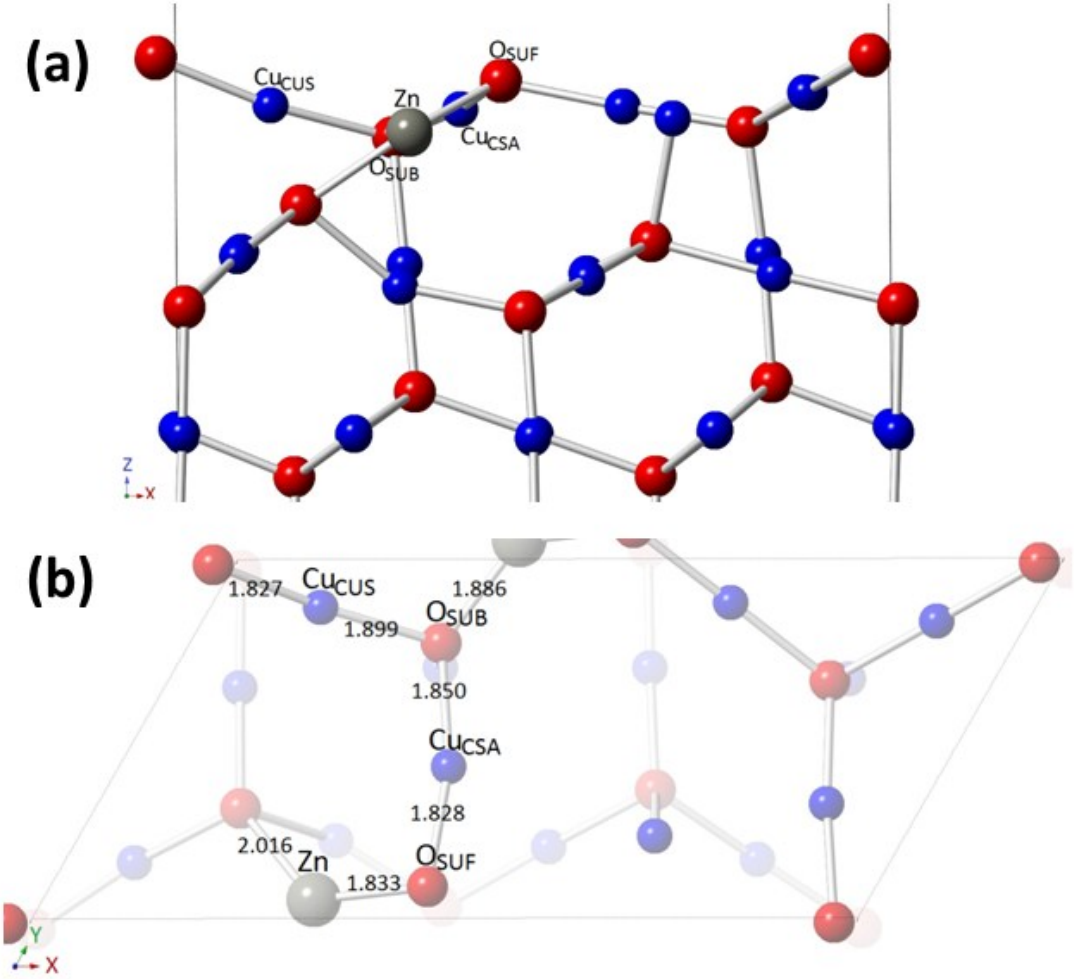

Figure S12. Side (a); and top (b) views of the Zn-doped (2×1) slab of the $Cu_2O(111)$-Cu_{vac} surface. Bond length values are in Å.

Table S1. Response and recovery times of the sensors based on doped copper oxide samples

		RTA525, 30% RH	RTA525, 90% RH	TA650, 30% RH	TA650, 90% RH
Response τ_r (s)	OPT 300°C	2.4	6.9	3.1	12.6
	OPT 400°C	1.4	5.4	1.9	8.5
Recovery τ_d (s)	OPT 300°C	3.6	19.3	5.8	24.1
	OPT 400°C	2.9	12.1	4.2	21.3

Table S2. Hydrogen gas sensors based on *p*-type metal oxide nanostructures

Structure, morphology and properties of sensing material	H_2 conc. (ppm)	Gas response (R_a/R_g)	Operating temperature (°C)	Ratio of H_2 to ethanol vapour response S_{H2}/S_{EtOH}	Year of publication	Ref.
Co_3O_4 nanotubes	50	~ 3 [a)]	30 (RT)	~ 0.85 [a)]	2005	15
NiO hollow hemispheres; D ~ 800 nm;	200	1.8	300	0.36	2011	16
Mesoporous CuO film: D ~ 30±10 nm; h ~ 200 nm;	100	1.65	300	~ 0.22 [a)]	2013	17
CuO urchin-like: D ~ 3 μm;	100	~ 6 [a)]	200	-	2013	18
$Zn_xCu_{1-x}O_y$ nano-crystalline films; D ~ 40-60 nm; h ~ 100 nm;	100	~8.5	300	~ 9.5	**Current work**	-

[a)]Denotes a value approximated from a graphical plot;

Data are sorted by the year of publication. Where were not available specific data is noted by "-". Average diameter of nanostructures is noted by "D" and thickness of films is noted by "h".

References

1. G. Kresse and J. Hafner, *Phys. Rev. B*, 1993, **47**, 558-561.
2. G. Kresse and J. Hafner, *Phys. Rev. B*, 1994, **49**, 14251-14269.
3. G. Kresse and J. Furthmüller, *Comput. Mater. Sci.*, 1996, **6**, 15-50.
4. G. Kresse and J. Furthmüller, *Phys. Rev. B*, 1996, **54**, 11169-11186.
5. P. E. Blöchl, *Phys. Rev. B*, 1994, **50**, 17953-17979.
6. J. P. Perdew, K. Burke and M. Ernzerhof, *Phys. Rev. Lett.*, 1996, **77**, 3865-3868.
7. J. P. Perdew, K. Burke and M. Ernzerhof, *Physical Review Letters*, 1997, **78**, 1396-1396.
8. S. L. Dudarev, G. A. Botton, S. Y. Savrasov, C. J. Humphreys and A. P. Sutton, *Phys. Rev. B*, 1998, **57**, 1505-1509.
9. A. K. Mishra, A. Roldan and N. H. de Leeuw, *J. Phys. Chem. C*, 2016, **120**, 2198-2214.
10. M. K. Yaakob, N. H. Hussin, M. F. M. Taib, T. I. T. Kudin, O. H. Hassan, A. M. M. Ali and M. Z. A. Yahya, *Integr. Ferroelectr.*, 2014, **155**, 15-22.
11. S. Grimme, *J. Comput. Chem.*, 2006, **27**, 1787-1799.
12. H. J. Monkhorst and J. D. Pack, *Phys. Rev. B*, 1976, **13**, 5188-5192.
13. G. Henkelman, A. Arnaldsson and H. Jónsson, *Comput. Mater. Sci.*, 2006, **36**, 354-360.
14. R. F. W. Bader, ed., *Atoms in Molecules: A Quantum Theory*, Oxford University Press, London, 1994.
15. W.-Y. Li, L.-N. Xu and J. Chen, *Adv. Funct. Mater.*, 2005, **15**, 851-857.
16. N. G. Cho, I.-S. Hwang, H.-G. Kim, J.-H. Lee and I.-D. Kim, *Sens. Actuators B*, 2011, **155**, 366-371.
17. Y.-H. Choi, D.-H. Kim, S.-H. Hong and K. S. Hong, *Sens. Actuators B*, 2013, **178**, 395-403.
18. D. P. Volanti, A. A. Felix, M. O. Orlandi, G. Whitfield, D.-J. Yang, E. Longo, H. L. Tuller and J. A. Varela, *Adv. Funct. Mater.*, 2013, **23**, 1759-1766.